Proceedings of the IASS 2024 Symposium
Redefining the Art of Structural Design
August 26-30, 2024, Zurich Switzerland
Philippe Block, Giulia Boller, Catherine DeWolf,
Jacqueline Pauli, Walter Kaufmann (eds.)

Probability Model of Non-linear Buckling Capacity of Single-Layer Reticulated Shells Using Constrained Stochastic Imperfection Modal Method

Chenyu WU, Shouchao JIANG, Shaojun ZHU*

* College of Civil Engineering, Tongji University
Room A708, College of Civil Engineering, Tongji University, No. 1239 Siping Road, Yangpu District, 200092 Shanghai. E-mail: zhushaojun@tongji.edu.cn

Abstract

Single-layer reticulated shells exhibit a remarkable sensibility to initial geometric imperfections in relation to their non-linear buckling characteristics. To thoroughly investigate the probability model of the non-linear buckling capacity of single-layer reticulated shells, this paper adopts the constrained stochastic imperfection modal method, which can effectively consider the topology constraint that existed in actual initial imperfection fields, to perform non-linear buckling analysis for single-layer spherical reticulated shells, considering different numbers of rings and imperfection amplitudes. The results show that the probability models of the non-linear buckling capacity of single-layer reticulated shells obtained by sampling with the constrained stochastic imperfection modal method exhibit significant discrepancies compared to that obtained by conventional random imperfection methods, which indicates the crucial necessity of considering structural topology constraints in the constrained stochastic imperfection modal method. Meanwhile, the evolution of the probability model also exhibited counter-intuitive variations that under different imperfection amplitudes, the form of the probability density function will also change. Furthermore, a physical parameter known as the joint well-formedness is introduced, quantifying the local stiffness of the joints. This physical parameter is found to have a profound and highly intertwined correlation with the structural non-linear buckling modes. By incorporating parameters of the joint well-formedness and the non-linear buckling deformation, a penetrative analysis of the characteristics of probability distributions with respect to imperfection amplitudes is conducted. As a result, recommendations for the allowable deviation of joints and determination schemes for critical joints during the construction process are proposed.

Keywords: single-layer reticulated shells, constrained stochastic imperfection modal method, non-linear buckling capacity, probability model, joint well-formedness.

1. Introduction

Single-layer reticulated shells (SLRSs) have gained significant popularity in long-span building structures since the 1950s due to their aesthetic appeal, superior mechanical performance, and efficient material utilization [1]. The safety of SLRSs is largely determined by their non-linear buckling capacity, which is significantly influenced by initial geometric imperfections (IGIs) of joints arising during the fabrication and installation processes [2, 3]. Specifically, minor IGI of joint deviations can result in a reduction of more than 50% in the non-linear buckling capacity of the structure [4].

In recent decades, scholars have been devoted to establishing initial imperfection fields to simulate IGIs that align with engineering realities. The prevalent methods for the simulation of IGIs, including the random imperfection method (RIM) [5], the consistent imperfection modal method (CIMM) [6], the

random field method (RFM) [7], and the eigenmode imperfection method (EIM) [8], yet these methods fail to accurately simulate the actual IGIs [1].

Based on the aforementioned imperfection simulation methods, numerous in-depth studies have been carried out on the non-linear buckling capacity of SLRS. Fan *et al*. [9] analyzed the differences in non-linear buckling capacity characteristics of SLRSs under three sampling methods: RIM, EIM, and CIMM, recommending EIM for its reduced computational demands. He *et al*. [10] employed the RIM to conduct non-linear buckling analyses of Kiewitt-6 SLRSs and provided the probability distribution characteristics of the non-linear buckling loads. Furthermore, Cui *et al*. [11] performed the reliability analysis of non-linear buckling capacity in the SLRS and cylindrical shell, and the probability distribution function of non-linear buckling capacity was obtained.

However, the characteristics of the non-linear buckling capacity of SLRSs obtained by the aforementioned research lack sufficient persuasiveness due to unrealistic IGI simulation methods. To simulate actual IGIs more accurately, the constrained stochastic imperfection modal method (CSIMM) [12] was proposed, which can effectively consider the topology constraint that existed in actual initial imperfection fields.

Obviously, investigating the probability distribution for non-linear buckling capacity has significant implications for the stability design of SLRSs based on more realistic IGIs obtained by CSIMM. This paper aims to establish the probability model of non-linear buckling capacity obtained by CSIMM and reveal its characteristics. Section 2 briefly introduces the CSIMM. The parametric analysis is performed in Section 3. Subsequently, Section 4 reveals the characteristics of probability models in conjunction with the joint well-formedness.

2. CSIMM method

CSIMM separates the consideration of the direction and magnitude of the deviation vector of joints in 3D space by conducting random sampling. Subsequently, virtual interaction forces (VIFs) are introduced so that the joint coordinates are updated iteratively by the forward Euler method, aiming to maintain inter-joint distances within specified limits. The specific steps are as follows:

S1. Generate stochastic 3D joint deviations by performing the Monte Carlo sampling. Specifically, the independent joint deviations in the x, y, and z directions follow a uniform distribution on the interval $[-1,1]$. The amplitude of joint deviation follows a truncated normal distribution, which is truncated at $\mu \pm 2\sigma$;

S2. Transfer the joint-member-joint structural model into an equivalent particle-spring-particle system and calculate the VIFs of the particles. The amplitude and direction of the VIFs are related to the extent that the topology constraint is violated. Details of the VIFs can be found in reference [12];

S3. Apply stochastic perturbations following a distribution described by S1, the joint coordinates are updated by generative VIFs. Multiple iterations are conducted until both the joint coordinates deviations and the member lengths deviations among the entire structure are within the specified tolerance limits.

3. Parameter analysis

As one of the most commonly used structural types, Kiewitt-6 (K6) steel SLRSs are adopted to perform parameter analysis in order to illustrate the evolution law of the probability model of structural non-linear buckling capacity.

3.1. Numerical model parameters

The numerical model of the K6 SLRS is established in the general finite-element analysis software package ABAQUS [13]. The geometric characteristic of the model is shown in Figure 1. The specific geometric or structural parameters or relevant information are as follows:

1. Number of rings: m = 8, 10, 12;
2. Span: L = 40 m;

3. Height: f = 10 m;
4. Imperfection amplitude: L/300, L/500, L/800, L/1000, L/1200, L/1500, L/3000;
5. IGIs simulation methods: CSIMM and RIM;
6. Support condition: pinned constraint. Note that constraint supports are only set at the outermost joints of the structure;
7. Member element: circular hollow section of Ø100×4 (unit: mm);
8. Material: Q345 steel;
9. Joint rigidity: fully rigid;
10. Load distribution: full-span dead load of 1.0 kN/m^2 and full-span live load of 0.5 kN/m^2.

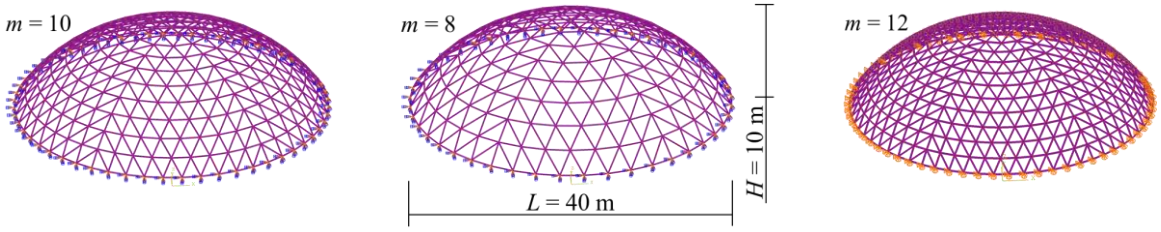

Figure 1: Numerical example parameter illustration

It is notable that the arc-length method is adopted in the non-linear buckling analysis of SLRSs.

3.2. Evolution laws of the probability distribution

To facilitate the description of their evolution laws, the parameter scenarios were numbered and referenced in Table 1. For each scenario of SLRS, 1000 IGIs are generated by CSIMM, i.e., 21,000 SLRSs with IGIs are analyzed to determine their non-linear buckling capacities. Subsequently, the probability density functions (PDFs) of buckling capacities are obtained by the kernel density estimation method [14].

Table 1: Parameter scenarios of SLRSs

Number of rings	Imperfection amplitudes (Number of scenarios)
8	L/300 (1), L/500 (2), L/800 (3), L/1000 (4), L/1200 (5), L/1500 (6), L/3000 (7)
10	L/300 (8), L/500 (9), L/800 (10), L/1000 (11), L/1200 (12), L/1500 (13), L/3000 (14)
12	L/300 (15), L/500 (16), L/800 (17), L/1000 (18), L/1200 (19), L/1500 (20), L/3000 (21)

For scenarios 4 and 5, 1000 IGIs are generated by RIM and CSIMM, respectively. A comparison of probability models obtained based on RIM and CSIMM is shown in Figure 2. It can be observed that the probability models of Λ obtained by the above two stochastic imperfection simulation methods have a significant discrepancy. As the PDF based on CSIMM exhibits the bimodal distribution, that based on RIM exhibits an unimodal distribution. The discrepancy indicates the crucial necessity of considering structural topology constraints in the CSIMM. Therefore, only the CSIMM is adopted as the IGI simulation method for further parametric analysis.

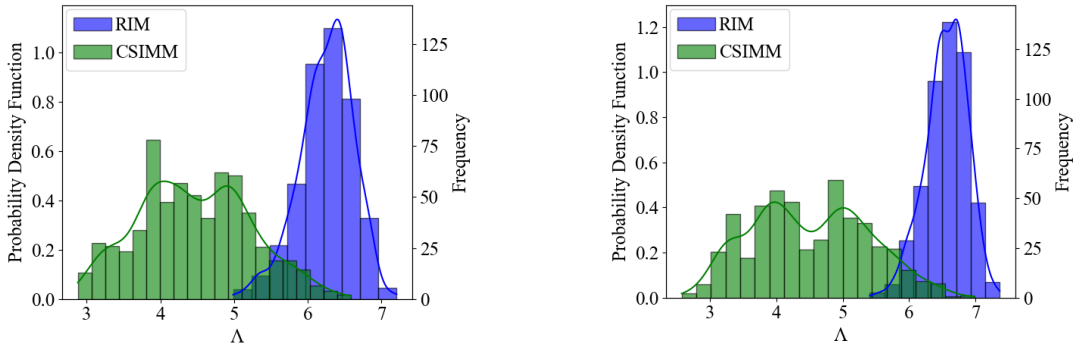

(a) Scenario 4 (b) Scenario 5

Figure 2: Comparison of probability models for scenarios 4 and 5 between RIM and CSIMM

Taking scenarios 1~7 of SLRSs as an example, the histogram and PDF curve of buckling capacities are shown in Figure 3. It is notable that the load factor Λ is introduced to describe the magnitude of non-linear buckling capacity, representing the multiplier relationship between the load condition and the ultimate load, i.e.,

$$\mathbf{Q}^{u} = \Lambda \mathbf{Q} \tag{1}$$

where $\mathbf{Q}^{u}$ is the ultimate buckling load, and $\mathbf{Q}$ is the load condition described in section 3.1.

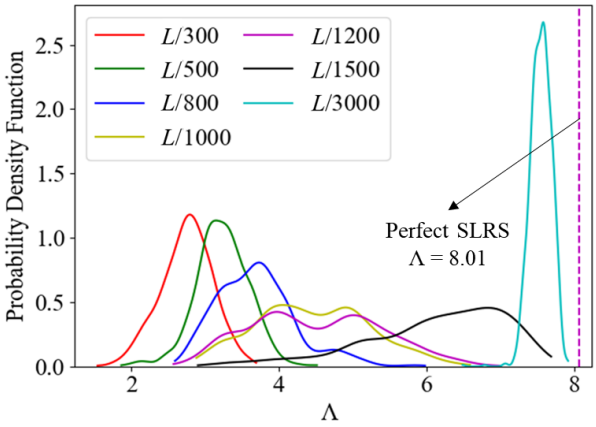

Figure 3: Non-linear buckling load factors PDFs under different imperfection amplitudes for scenarios 1~7

From Figure 3, some interesting phenomena can be discovered:

1) Under smaller imperfection amplitudes (L/3000), the probability model of Λ of SLRSs approximates a skewed distribution, with the samples concentrated in a relatively narrow range of Λ.
2) As the imperfection amplitudes of SLRSs increase (L/1500, L/1200, L/1000, and L/800), the probability model exhibits two peaks, and the PDFs become more extensive.
3) With further increases in imperfection amplitudes (L/500, L/300), the probability model approximates the normal distribution.
4) Compared to scenarios 3~6 (L/1500, L/1200, L/1000, and L/800), the PDFs of scenarios 1, 2, and 7 exhibit greater concentration.

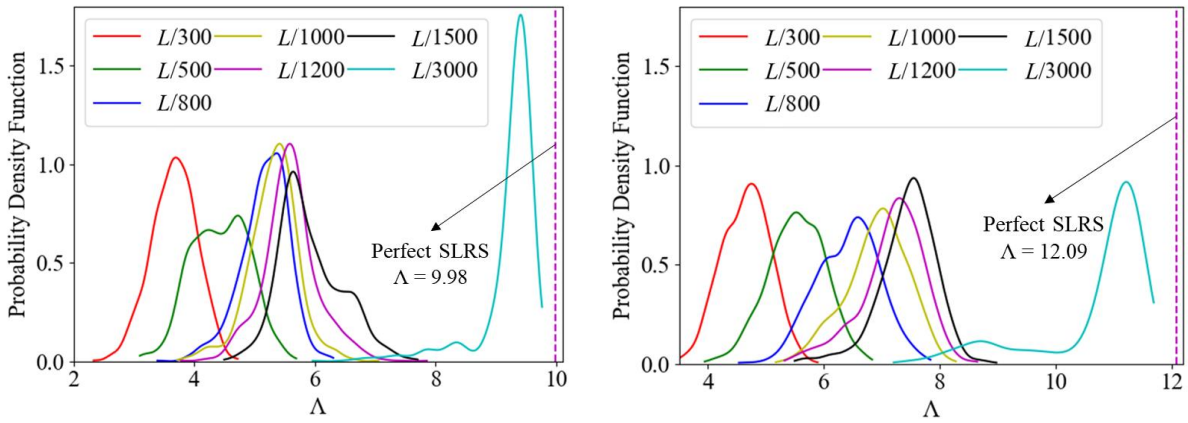

(a) Scenarios 8~14 (b) Scenarios 15~21

Figure 4: Non-linear buckling load factors PDF under different imperfection amplitudes for scenarios 8~14 and scenarios 15~21

For scenarios 8~14 and scenarios 15~21, their PDF curves of buckling capacities are shown in Figure 4. It can be observed that as the imperfection amplitudes decrease, the trend of variation in the PDF curves exhibits a remarkable degree of similarity to that of scenarios 1~7. The detailed trend of variation will

be elucidated in Section 5. However, in comparison to scenarios 1~7, no distinctive bimodal distribution is apparent.

4. Evolution mechanism of probability models

On the basis of probability models of K6 SLRSs in Section 3, this section aims to reveal the inherent mechanism of the evolution of the non-linear buckling capacity probability models.

4.1. Joint well-formedness

In order to facilitate further analysis, the concept of joint well-formedness proposed in reference [15] is first introduced. For an SLRS in 3D space with n joints, its global stiffness matrix $\mathbf{K}$ can be expressed as an $n \times n$ sub-matrix, i.e.

$$\mathbf{K} = \begin{bmatrix} \mathbf{K}_{11} & \cdots & \mathbf{K}_{1n} \\ \vdots & \mathbf{K}_{kk} & \vdots \\ \mathbf{K}_{n1} & \cdots & \mathbf{K}_{nn} \end{bmatrix} \tag{2}$$

where $\mathbf{K}_{kk}$ is the symmetric positive definite matrix that describes the stiffness of the kth joint. Its dimensionality, denoted by C, is equal to the number of degrees of freedom associated with the joint.

To evaluate the local stiffness of each joint of SLRSs, the concept of joint well-formedness is introduced. The formulation of the joint well-formedness of kth joint q_k is presented below to quantify this relationship explicitly:

$$q_k = \det\left(\mathbf{K}_{kk}\right) = \prod_{i=1}^{C} \lambda_i \tag{3}$$

where λ_i ($i = 1,2,3,\cdots,C$) is the eigenvalue of $\mathbf{K}_{kk}$.

This metric relies solely on the intrinsic connection strength at the kth joint, reflecting the topological relationship inherent within the structure. It is worth noting that the local stiffness of the kth joint enhances as the magnitude of the value of q_k increases.

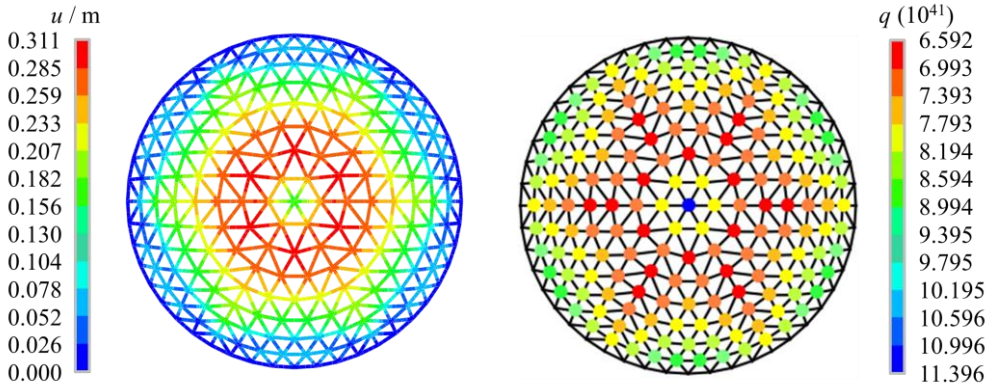

Figure 5: Comparison between the non-linear buckling deformation and the initial joint well-formedness of joints of perfect structure (m = 8)

A comparison between the initial joint well-formedness of perfect SLRS (m = 8) and its non-linear buckling deformation diagram is shown in Figure 5. It reveals that the magnitude of deformation during structural buckling perfectly aligns with the size of their initial joint well-formedness, and the two physical quantities exhibit a strong correlation. It is worth noting that since the outermost ring joints of SLRSs are constrained by supports, and there is no initial deviation in joint coordinates, their joint well-formedness is not considered.

4.2. Classification of non-linear buckling deformation pattern

Through in-depth analyses, the non-linear buckling deformation patterns (BDPs) obtained by CSIMM can be divided into five types, as illustrated in Figure 6. These comprise local indentation at the inner ring joints of primary ribs (Pattern 1), local indentation at the inner ring joints of non-primary ribs (Pattern 2), local indentation at the outer ring joints of primary ribs (Pattern 3), local indentation at the outer ring joints of non-primary ribs (Pattern 4), and global indentation (Pattern 5). Notably, the inner ring refers to the number of rings less than or equal to half of *m*. Moreover, Patterns 1~4 can be combined to lead to hybrid failure patterns, i.e., multiple local area indentation.

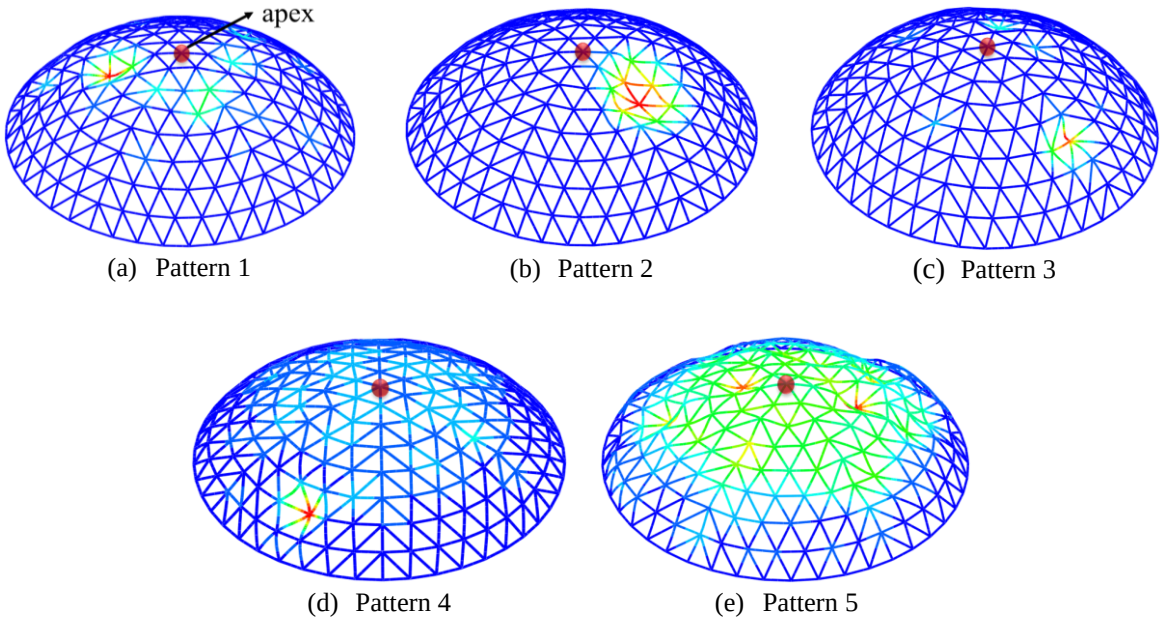

Figure 6: Non-linear buckling deformation patterns of SLRSs

4.3. Characteristics of normal distribution

As shown in Figure 3, scenarios 1 and 2 exhibit a normal distribution of the PDF of Λ. Taking scenario 1 as an example, the characteristics of its probability model are analyzed. For descriptive purposes, the feature points *A*, *B*, and *C* are selected in the low, medium, and high range of Λ, respectively, as shown in Figure 7.

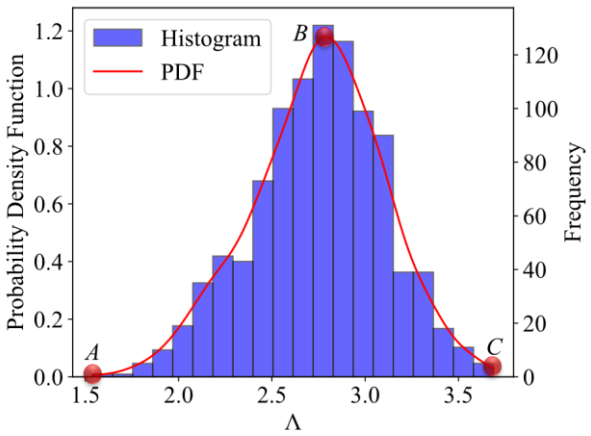

Figure 7: Histogram and PDF of non-linear buckling load factors of scenario 1

The characteristic of scenario 1, along with the conclusions drawn from a thorough analysis of this characteristic, can be summarized as follows:

1. The BDPs near point *A* are predominantly Pattern 1, where the initial deviations at the joints of the primary ribs within the SLRSs of this region are significantly larger than those of the surrounding areas, resulting in an excessively low local stiffness (refer to Figure 8). The structure succumbs to local indentations at joints of insufficient stiffness before the global resistance potential can be mobilized, leading to buckling;
2. From point *A* to point *B*, as the frequency increases, the BDPs progressively enrich. The BDPs, such as Patterns 2, 3, and 4, and their combinations, start to manifest. For the samples of this range, joints with significant initial deviations increasingly proliferate, leading to an augmentation in joints characterized by diminished joint well-formedness (refer to Figure 8). Closer proximity to point *B* correlates with a richer diversity of BDP obtained for the same Λ, thereby elevating the frequency, which culminates in a peak at point *B*;
3. From point *B* to point *C*, samples predominantly show local indentations at the inner ring joints (Patterns 1 and 2), with fewer samples of outer ring joint indentations. The local stiffness of inner ring joints tends to be lower than that of other joints within a single sample, but the global stiffness of joints is higher than that of point *B* (refer to Figure 8), resulting in a higher section of Λ compared to the previous samples;
4. When sampling with large initial imperfection amplitudes such as *L*/300, significant initial joint deviations that adversely affect local stiffness occur, resulting in a generally lower Λ. Consequently, Pattern 5 does not occur, indicating an inability to fully utilize the structural potential to resist external loads.

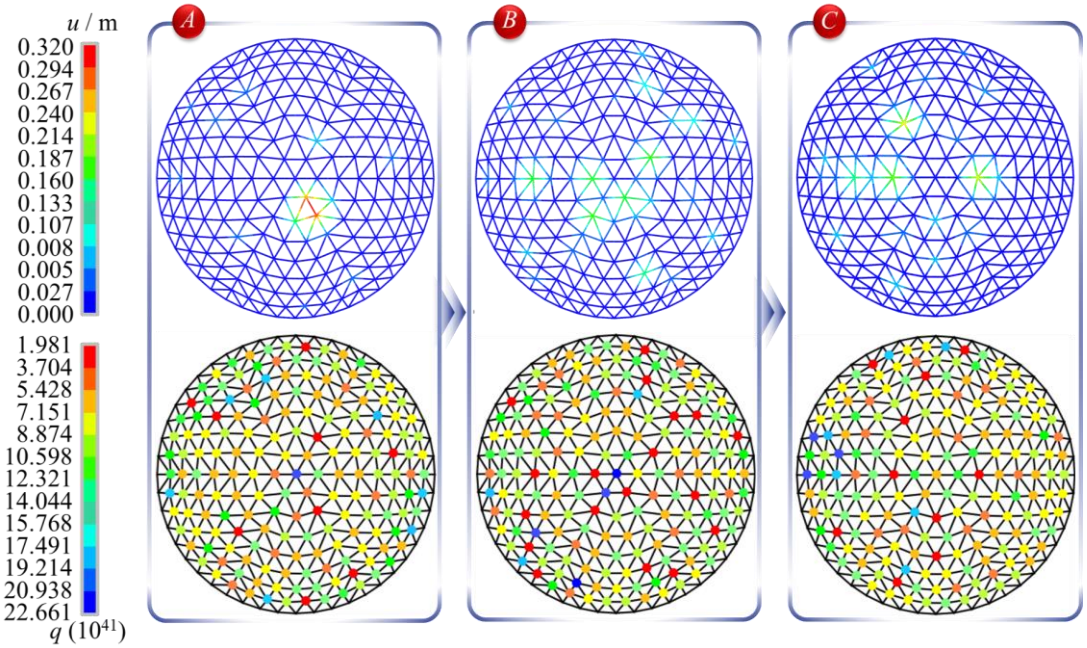

Figure 8: Scenario 1's representative samples of non-linear buckling deformations and the initial joint well-formedness.

4.4. Characteristic of bimodal distribution

Scenario 4 is taken as an example to reveal the characteristics of bimodal distribution. Similar to Section 4.3, the feature points *A*, *B*, *C*, *D*, and *E* are selected in the low range of Λ, medium range of Λ, and high range of Λ. It is notable that the medium range of Λ selects points *B*, C, and *D* as the feature points, representing the three extreme points, as shown in Figure 9.

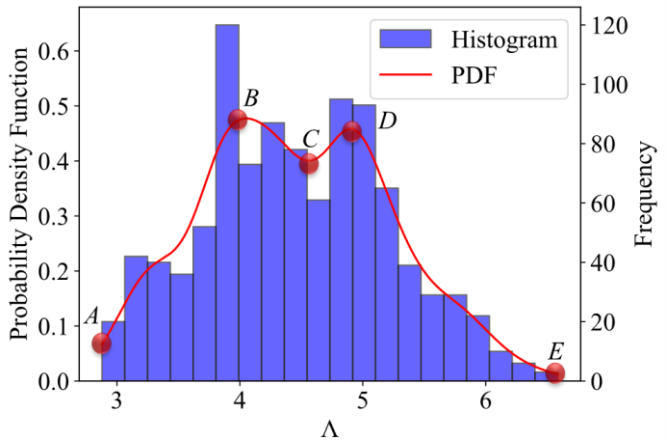

Figure 9: Histogram and PDF of non-linear buckling load factors of scenario 4

The characteristic of scenario 4, along with the conclusions drawn from a thorough analysis of this characteristic, can be summarized as follows:

1. Between points *A* and *B*, the BDPs within SLRS samples transition from local indentation at the inner ring joints (Patterns 1 and 2) to Pattern 5. Throughout this transition, the joint well-formedness within the structure progressively expands from an overly small single joint in the inner ring to a more extensive assembly comprising multiple joints, thereby forming a global configuration (refer to Figure 10). Approaching point *B*, there emerges a phenomenon where an undersized joint well-formedness in a minority of the outer ring joints leads to local indentations at these outer ring joints.
2. Between points *B* and *C*, Patterns 1 and 2 are almost non-existent, while Pattern 5 dominates. The quantity of Pattern 3 is minimal, while Pattern 4 noticeably increases. The number of joints with small joint well-formedness in the SLRSs gradually increases. The occurrence of a single joint in the inner ring with significantly smaller joint well-formedness compared to its surroundings is almost absent, while the occurrence of one or multiple joints with undersized joint well-formedness of outer ring joints starts to increase (refer to Figure 10).
3. Between points *C* and *D*, there is an increase in the quantity of Pattern 3, and the dominant BDPs in this region are Patterns 3, 4, and 5. Compared to the previous region, there is a significant increase in samples exhibiting local indentations due to undersized joint well-formedness of the outer ring joints of primary ribs (refer to Figure 10). This leads to a higher diversity of BDPs, resulting in the emergence of a second peak.
4. Between points *D* and *E*, there is a gradual reduction in the occurrence of Patterns 3 and 4, ultimately leaving only Pattern 5. In this region, the joint well-formedness in each sample exhibits a generally moderate and uniform configuration (refer to Figure 10). This characteristic is favorable for fully utilizing the global resistance capacity of the structure, resulting in higher Λ.
5. In the low range of Λ, the majority of samples exhibit local indentation at the inner ring joints, indicating the large deviations in inner ring joints have a greater impact on Λ than those in outer ring joints. Consequently, during the construction and acceptance of SLRSs, particular attention should be given to deviations in the inner ring joints from their designated positions.
6. For the SLRS sample with Pattern 3 at point *D* (refer to Figure 10), it can be observed that there are two outer ring joints with significantly larger displacements at the non-linear buckling moment. The displacement at the primary rib joint is noticeably larger than that at the non-primary rib joint. However, the initial joint well-formedness (i.e., local stiffness of the joint) at the primary rib joint is larger than that at the non-primary rib joint. This indicates that compared to the non-main rib joints, the deviations at the main rib joints have a more pronounced influence on Λ of the SLRS. Consequently, during the construction and acceptance of SLRSs, particular attention should be given to deviations in primary rib joints from their designated positions.

4.5. Characteristics law of skewed distribution

Scenarios 6 and 7 exhibit a skewed distribution (refer to Figure 3). The BDPs of the SLRS samples in these two scenarios are all Pattern 5. The joint well-formedness in the SLRSs exhibits a global uniform magnitude without localized excessive or insufficient values. This is attributed to the smaller initial deviations of each joint when the imperfection amplitude is low. As a result, the range of Λ obtained is significantly larger than that of scenarios 1~5. When the imperfection amplitude does not exceed $L/1500$, it can be almost guaranteed that randomly sampled imperfect structures can fully utilize their global resistance capacity.

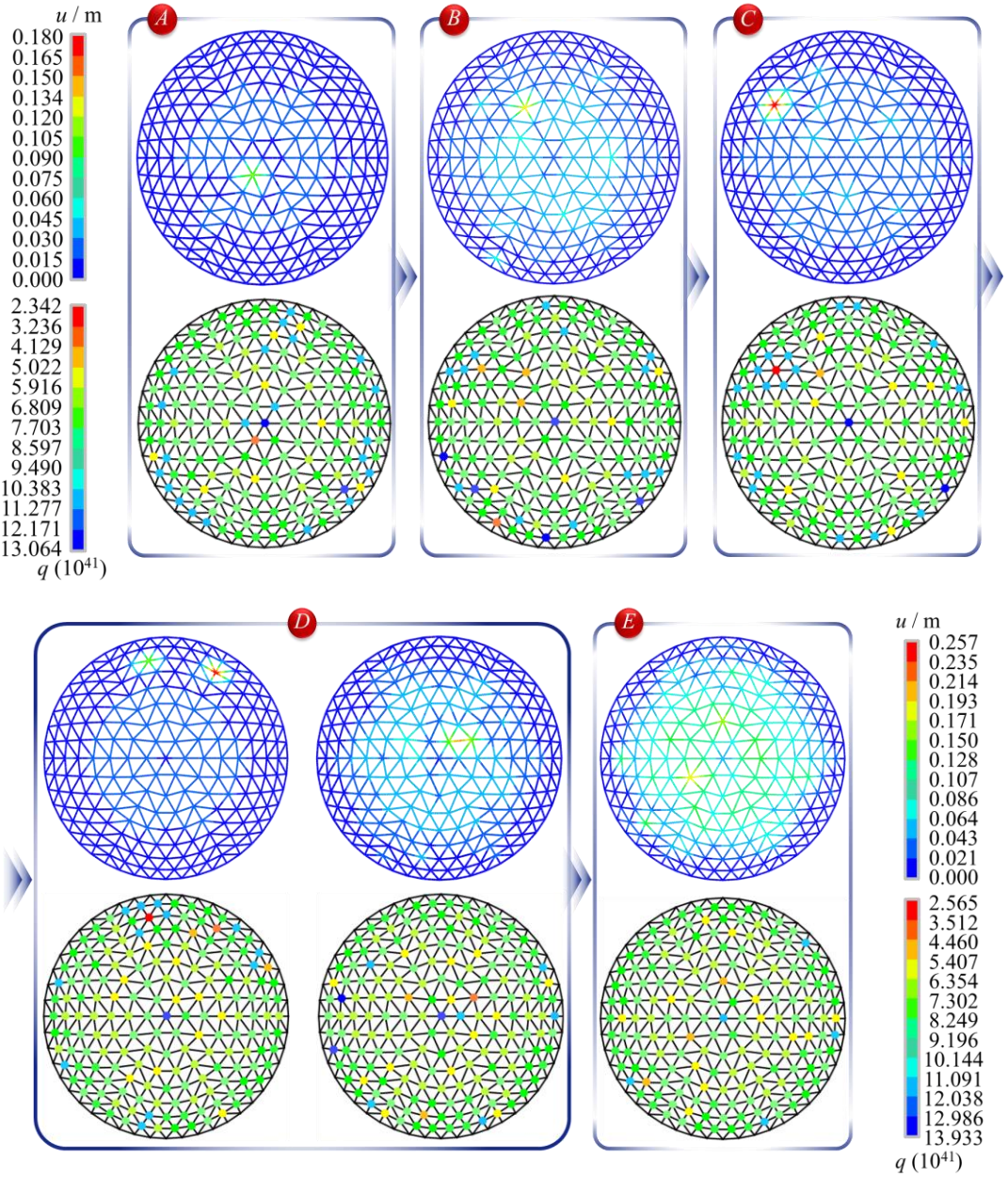

Figure 10: Scenario 4's representative samples of non-linear buckling deformations and the initial joint well-formedness.

5. Conclusion

This study investigates the non-linear buckling behavior of randomly generated initial imperfect structures obtained through CSIMM sampling by varying parameters such as imperfect amplitudes and number of rings. The conclusions drawn from the analysis are as follows:

- Under the same imperfection amplitude, the probability models obtained through CSIMM show significant differences compared to those obtained through the traditional random imperfection method. Furthermore, the probability models for the non-linear buckling capacity obtained through CSIMM exhibit significant variations across different imperfection amplitudes. As the imperfection amplitude decreases to $L/3000$ (with L being the structural span), the mean value of the PDF gradually increases, while the standard deviation initially increases and then decreases.
- The initial joint well-formedness exhibits an extremely strong correlation with the corresponding non-linear buckling displacement of the joints in the SLRS. The generation of initial deviation at each joint influences its local stiffness, thereby exerting an impact on the non-linear buckling mode. As a consequence, variations in the non-linear buckling capacity occur.
- The potential non-linear buckling modes of K6 SLRSs can be divided into five types: local indentation at the inner ring joints of primary ribs (Pattern 1), local indentation at the inner ring joints of non-primary ribs (Pattern 2), local indentation at the outer ring joints of primary ribs (Pattern 3), local indentation at the outer ring joints of non-primary ribs (Pattern 4), and global indentation (Pattern 5). Notably, the inner ring refers to the number of rings less than or equal to half of m. Moreover, Patterns 1~4 can be combined to lead to hybrid buckling modes, i.e., multiple local area indentation.
- When the imperfection amplitude is set to a large value ($L/300$, $L/500$), the majority of SLRS samples exhibit local indentations as their dominant BDPs, failing to fully utilize the structural global resistance capacity. When the imperfection amplitude is moderate ($L/800$, $L/1000$, $L/1200$), with the increase of Λ, the BDPs transition from predominantly Pattern 1 to the presence of all five patterns. As Λ reaches a higher value range, the BDPs mainly consist of Patterns 4 and 5. For smaller imperfection amplitudes ($L/1500$, $L/3000$), almost all SLRS samples exhibit global indentations as their BDPs. Consequently, it is recommended to consider the imperfection amplitudes within the range of $L/1500$ in order to fully utilize structural global resistance capacity.
- By integrating the analysis of the joint well-formedness, it has been observed that the detrimental effect of significant deviations in primary rib joints is more pronounced on the buckling capacity compared to significant deviations in non-primary rib joints. Similarly, large deviations in inner ring joints have a greater impact on the buckling capacity than those in outer ring joints. During the construction of SLRSs, particular attention should be given to deviations in primary rib joints and inner ring joints from their designated positions. Reinforcement measures may be implemented as deemed necessary.

Generally speaking, this research provides a new paradigm of the non-linear buckling capacity probability model for SLRS, and the frequently utilized K6 SLRS in practical engineering is presented in this study to illustrate the workflow of this research paradigm. This study furnishes a scientific foundation for unifying the design and acceptance theory with the underlying logic of SLRSs, thereby offering a reference and basis for research on other topology types of SLRSs.

References

[1] S. Zhu, Q. Zeng, X. Yang, and C. Wu, "State-of-the-art review of initial imperfection field simulation methods for single-layer gridshells," *Proceedings of the IASS Annual Symposium*, Melbourne: International Association for Shell and Spatial Structures, 2023, pp. 1-12.

[2] H. Li, C. Wang, and Y. Xiao, "Effect of random nodal deviation and member eccentricity on load-carrying capacity of single-layer dome," *Journal of Building Structures*, vol. 41, no. 2, pp. 134-141, 2020. (in Chinese)

[3] Z. Sadovskýa and J. Kriváček, "Influential geometric imperfections in buckling of axially compressed cylindrical shells – A novel approach," *Engineering Structures*, vol. 223, pp. 111170, 2020.

[4] F. Fan, J. Yan, and Z. Cao, "Elasto-plastic stability of single-layer reticulated domes with initial curvature of members," *Thin-Walled Structures*, vol. 60, pp. 239–246, 2012.

[5] S. Shen and X. Chen, *Stability of Reticulated Shell Structures*, Beijing: China Science Publishing& Media Ltd, 1999. (in Chinese)

[6] X. Chen and S. Shen, "Load-displacement process and imperfection analysis of single-layer geodesic domes," *Journal of Building Structures*, vol. 13, no. 3, pp. 11-18, 1992. (in Chinese)

[7] G. Chen, H. Zhang, K. J. R. Rasmussen, and F. Fan, "Modeling geometric imperfections for reticulated shell structures using random field theory," *Engineering Structures*, vol. 126, pp. 481-489, 2016.

[8] Z. Cao, *Elastic-plastic stability of reticulated shells*, Harbin: Harbin Institute of Technology, 2007. (in Chinese)

[9] F. Fan, Z. Cao, and S. Shen, "Elasto-plastic stability of single-layer reticulated shells," *Thin-Walled Structures*, vol. 48, pp. 827-836, 2010.

[10] S. He, Z. Jiang, and J. Cai, "Investigation on simulation methods of initial geometric imperfection distribution in elasto-plastic stability analysis of single-layer reticulated shells," *KSCE Journal of Civil Engineering*, vol. 22, no. 4, pp. 1193-1202, 2018.

[11] X. Cui, Y. Li, and H. Hong, "Reliability of stability of single-layer latticed shells with spatially correlated initial geometric imperfection modeled using conditional autoregressive model," *Engineering Structures*, vol. 201, pp. 109787, 2019.

[12] Q. Zeng, X. Guo, X. Yang, S. Zhu, and Z. Li, "Constrained stochastic imperfection modal method for nonlinear buckling analysis of single-layer reticulated shells," *Journal of Structural Engineering*, vol. 149, no. 3, pp. 04022265, 2023.

[13] Dassault Systèmes, *Abaqus 2021*. Providence, RI: Dassault Systèmes, 2021.

[14] E. García-Portugués, *Notes for Nonparametric Statistics*, Version 6.9.0, ISBN 978-84-09-29537-1, 2023.

[15] J. Ye, W. Liu, and R. Pan, "Research on failure scenarios of domes based on form vulnerability," *Science China Technological Sciences*, vol. 54, pp. 2834-2853, 2011.